PAPER • **OPEN ACCESS**

1.5 GHz non-invasive directional deep brain stimulation with improved focus size and minimized input power

To cite this article: Chen Xue and Alex M H Wong 2025 *J. Neural Eng.* **22** 046049

Journal of Neural Engineering

PAPER

1.5 GHz non-invasive directional deep brain stimulation with improved focus size and minimized input power

Chen Xue[1] and Alex M H Wong[1,2,*]

[1] Department of Electrical Engineering, City University of Hong Kong, Hong Kong Special Administrative Region of China, People's Republic of China
[2] State Key Laboratory of Terahertz and Millimeter Waves, City University of Hong Kong, Hong Kong Special Administrative Region of China, People's Republic of China
[*] Author to whom any correspondence should be addressed.

E-mail: alex.mh.wong@cityu.edu.hk

Keywords: deep brain stimulation, 3D realistic head model, temporal interfering stimulation, microwave, *E*-field steerability, temperature analysis, SAR analysis

OPEN ACCESS

RECEIVED
7 March 2025

REVISED
3 August 2025

ACCEPTED FOR PUBLICATION
12 August 2025

PUBLISHED
26 August 2025

Abstract

Objective. Temporal interference stimulation (TIS) has recently been introduced for non-invasive deep brain stimulation (NDBS). While numerous studies have highlighted its advantages over conventional technologies, TIS still encounters challenges such as limited resolution and a lack of validation using human-like models. This article introduces an innovative method for NDBS which alleviates the resolution limit. *Approach.* We utilize as our excitation a 1.5 GHz microwave carrier modulated by a 10 Hz envelope. The microwave carrier enables strong electromagnetic focusing while the envelope triggers neural activity. To form this excitation, two dipole antenna arrays are placed around the head for the generation of *y*- and *z*-directed electric fields (*E*-field). Current excitations to the antenna arrays are tuned to control (i) the *E*-field to the desired focality position and (ii) its direction at the focality position. Full-wave simulations with a realistic head model are conducted to demonstrate the method. *Main results.* In the deep brain region, the cross-sectional focality sizes (75% threshold) are 0.73 cm^2, 1.18 cm^2 and 2.45 cm^2 in the *XOY, YOZ* and *XOZ* planes, respectively. The focality is much smaller than previously reported in the conventional method with kHz carrier waves. Further, the *E*-field direction at the focality can be steered along the *yz*-plane by adjusting the excitation weights of the antenna arrays. Multiphysics simulations on temperature distribution and specific absorption rate (SAR) show that the maximum temperature increase within a 30-minute stimulation session is 0.76 °C and the maximum SAR_{1g} is 2.70 W kg^{-1}. Both measures are within commonly accepted safe operation ranges. *Significance.* Compared to conventional TIS methods that utilize kHz carrier signals, our proposed approach achieves drastically improved spatial resolution and enables precise steering of the *E*-field. The proposed work holds significant potential for clinical applications, offering enhanced resolution and reduced input power for NDBS.

1. Introduction

For decades, the emergence and development of non-invasive deep brain stimulation (NDBS) have driven technological advancements and progress in both fundamental and clinical brain sciences. NDBS is a minimally invasive brain treatment procedure which can address a variety of pathological conditions, ranging from motor to cognitive disorders. During the treatment, electrodes, antenna arrays, or coils are used to target a specific region of a patient's brain to treat disorders such as epilepsy [1, 2], Parkinson's disease [3, 4], dystonia [5, 6], essential tremor [7, 8], and Tourette syndrome [9, 10]. By delivering the electromagnetic (EM) field to the lesion area, membrane polarization is altered, allowing for the potential propagation [11, 12] or blockage [13] of action potentials along

the axons, thereby enhancing brain function in a rapid, direct, and infection-free manner. Thus, interest in safe, efficient, accurate NDBS has grown dramatically.

Transcranial magnetic stimulation (TMS) and transcranial direct current stimulation (tDCS) are the main technologies of non-invasive brain stimulation [14]. These techniques have been extensively used as research tools in neurophysiology. TMS works by inducing a single pulse of strong magnetic field via a coil, which transfers energy across the brain tissue to generate a secondary electric current at the targeted region [15]. This induced electric current can trigger the action potential of neurons, thereby facilitating the treatment of neurological diseases. In contrast, tDCS involves the application of a weak direct current with constant polarization through electrodes, which does not induce action potentials but instead shifts neuronal resting membrane potentials to achieve depolarization [16, 17]. However, both methods are primarily effective for treating the brain cortex, which is relatively close to the skull. They are limited in their ability to target deep brain regions due to poor spatial resolution and insufficient penetration depth [14].

Temporal interference stimulation (TIS), a novel transcranial electrical stimulation, has recently been proposed for NDBS [18]. TIS utilizes multiple high-frequency electric field (*E*-field) signals with slight frequency shifts to generate a synthesized *E*-field with a low-frequency envelope at the targeted region [12, 18, 19]. TIS is feasible due to the intrinsic lowpass property of neuron membrane [18, 19]. Moreover, the nonlinear dynamics of ion channels enable the membrane to rectify signal envelopes [12]. In addition, most neurons share a similar voltage threshold for action potential generation [20–23], suggesting that large-scale adjustments to the input power are unnecessary for effective neural stimulation. Overall, the use of the proposed frequency is considered neurologically compatible. However, TIS faces a challenge in generating a high-resolution excitation focality, as the high-frequency signal typically needed to generate high-resolution hotspots is greatly attenuated by the brain tissue [18, 24]. To date, most studies in TIS have employed kHz-range carrier waves to mitigate power loss incurred at high frequencies [12, 18, 19]. Although the kHz signal ensures sufficient penetration depth, they offer limited resolution. Recently, Ahsan *et al* introduced a novel TIS approach using 1.5 GHz EM waves as the carrier wave [24]. To avoid signal attenuation, the antenna arrays were placed endocranially, which limits the practical applicability of the research. Oh *et al* proposed using a 6.5 GHz carrier wave with a 1 Hz envelope to stimulate hippocampal neurons in mice [25]. While this method successfully stimulated neurons, the fact that the work was done on mice, which have significantly different size and morphology compared to the human brains. An experimental validation of human-like model is necessary due to the aforementioned differences make that the animal experiment cannot perfectly represent the outcome of the human trials. Besides, there is a big gap between the safety considerations for humans [26] and the welfare for animals [27], which will influence the input power of the system.

Beside stimulation accuracy and penetration depth, minimizing the EM power emanating onto the brain, while actuating the desired neural activity at the desired location, is also a vital factor for DBS. Research on axon fiber tracts, which connect neurons and form neural networks, is crucial for power input of NDBS, as these tracts serve as signal pathways for brain functions [28–30]. Studies of Bikson *et al* on the activation strength of the *E*-field for neurons have shown that uniform steady-state extracellular fields beyond a threshold strength can excite neuron activity [31]. Deans *et al* noted that, compared to static *E*-fields, sinusoidal *E*-fields have smaller effects on transmembrane potentials, with sensitivity decreasing exponentially with frequency [32]. At 10 Hz, the effect is similar to that of DC fields, while at 50 and 60 Hz, it is approximately 0.4 times that of DC fields. Additionally, numerous studies [18, 33–37] on TIS deep brain stimulation have employed a 10 Hz envelope signal, further establishing that 10 Hz is recognized as a standard envelope frequency within the industry. For EM excitation with a fast carrier but much slower beat frequency [12], shows that the membrane of the neuron has a field rectifying effect, thus observing the excitation as a signal at the beat frequency. Finally it has been demonstrated that when the *E*-field orientation is parallel to axons in the hippocampus, the power required to evoke seizure-like events is halved compared to when the *E*-field is perpendicular to the axons [31]. Piecing this together, we see that non-invasively exciting the brain at (a) a high carrier frequency, (b) a reasonable beat frequency and (c) a direction-controlled, focused electric-field hotspot will allow us to selectively excite neurons with a high-resolution and minimal excitation power, resulting in successful neural stimulation with minimal unwanted exposure.

The analysis of the heating effects induced by EM waves is crucial. According to the International Electrotechnical Commission (IEC) standard, the maximum SAR_{10g}, which represents the amount of radiation absorbed by 10 g of human tissue, must remain within the safety limit of 10 W kg^{-1} [26]. As highlighted in [38], the maximum safe temperature for normal human tissue is approximately 43 °C; exceeding this threshold can cause thermal damage to cells, and prolonged exposure may result in cell

death. Various studies indicate that if the temperature increase induced by the proposed method is kept below 1 °C, it remains under the threshold for tissue damage or patient discomfort [39–43].

In this paper, we study the feasibility of enhancing the focal resolution of a TIS signal by applying an *E*-field TIS excitation with a GHz-range carrier on a realistic human head model. We present a dual antenna array based on the TIS that utilizes a 1.5 GHz frequency field to explore the feasibility of smaller focality and the safety of EM fields on brain tissue. Inspired by the importance of axon tracts, we investigate and achieve the steerability of the *E*-field to reduce power input, making our method safer and more efficient. In conclusion, this paper proposes a novel NDBS method based on TIS theory using a realistic human head model, marking a significant advancement for future clinical applications due to its pioneering use of steerable *E*-fields at microwave frequencies.

2. Method

2.1. Realistic head model

Computational models incorporating virtual human bodies which encompass mathematical, physical and anatomical information are indispensable for bio EM research. The Visible Human Project (VHP) Female computational human model, based on the finite element method (FEM), is an anatomically accurate, heterogeneous, surface-based human body model. FEM is a numerical technique employed to solve complex engineering problems involving partial differential equations by decomposing them into smaller, simpler elements, enabling accurate solutions to be computed using computers. In this work, we use commercial softwares HFSS and COMSOL to perform full-wave simulations on the EM fields inside the human head and the corresponding thermal effects. While the FEM can be computationally intensive, particularly for high-frequency full-wave analysis, we obtain drastic computational efficiency improvement by coupling it with a powerful adaptive mesh refinement procedure, which ensures accurate simulation results while significantly reducing computational runtime. In this study, we utilized the Static VHP-Female model v2.2 [44, 45], a truncated version of the VHP-Female model v3.0 BASE, excluding individual muscles. The v2.2 model has been evaluated by a board of medical experts and has over 500 registered users. The VHP-Female model v2.2 does not have the high resolution of VIP or MIDA models [46], but it is sufficient to obtain accurate simulation results by using the FEM method with adaptive mesh refinement technique. Furthermore, the resolution of the more complicated models is currently excessive for our research, as the simulation frequency is 1.5 GHz, corresponding to a wavelength of approximately 25 mm in the head model. This implies that highly detailed features have a negligible impact on the simulation results [47].

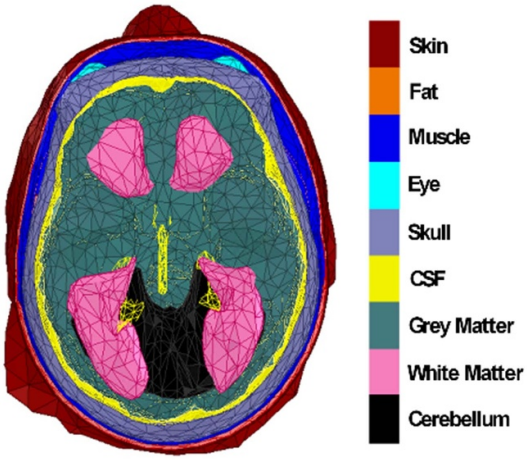

Figure 1. Axial cross-section of the realistic head model. Tissues in the applied realistic head model are shown in different colors.

The realistic head model is introduced into the full-wave simulation software Ansys HFSS EM solver and the multi-physics simulation software COMSOL, both of which are based on the FEM. Given a known set of sources, materials, and boundary conditions within the simulation domain, the FEM is employed to solve Maxwell's equations to determine the RF electric and magnetic fields within the domain, which in this case is the realistic human head model. The head model is comprised of nine types of tissues, as illustrated in figure 1: cerebellum, white matter, grey matter, cerebrospinal fluid (CSF), skull, muscle, fat, skin, and eyes. Each tissue is assigned specific electrical and thermal properties, which are detailed in section 2.3 following the frequency selection.

2.2. Multi-physics simulation

EM simulations are conducted in the frequency domain to calculate the *E*-field's spatial distribution within the head model based on the governing equation

$$\nabla \times \mu_{\mathrm{r}}^{-1} (\nabla \times \boldsymbol{E}) - k_0^2 \left(\varepsilon_{\mathrm{r}} - \frac{j\sigma}{\omega \varepsilon_0} \right) \boldsymbol{E} = 0 \qquad (1)$$

where μ_{r} is the relative permeability, $\boldsymbol{E}$ is the *E*-field, k_0 is the free-space wave number, ε_{r} is the relative permittivity, σ is the conductivity of the tissues, ω is the angular frequency, ε_0 is the free space permittivity. specific absorption rate (SAR) is calculated by equation (2) in frequency domain

$$\mathrm{SAR} = \frac{\sigma |\boldsymbol{E}|^2}{2\rho} \qquad (2)$$

where ρ is the density. The thermal effects of EM waves in the brain tissues are simulated in the time

domain by equations

$$Q_e = \frac{1}{2}\mathrm{Re}\left(\boldsymbol{J}\cdot\boldsymbol{E}^*\right) \tag{3}$$

where Q_e is the energy of E-field, $\boldsymbol{J}$ is the conductive current in the brain tissue. The energy associated with the magnetic field is not included here, as brain tissue is nonmagnetic. Finally, by substituting Q_e in to the Pennes' bioheat equation [48, 49]

$$\rho\cdot C\cdot\frac{\partial T}{\partial t}+\nabla\cdot(-k\nabla T)=Q_e \tag{4}$$

where ρ is the density, C is heating capacity, T is the temperature, t is time, we can get the temperature distribution in the head model. For simplicity, we have chosen to represent the tissues in the head model as solids. In this model, heat diffusion within the head and thermal radiation into the ambient environment serve as the cooling mechanisms. However, in actuality, blood perfusion will also help regulate the body temperature [50]. Hence the simulated temperature rise we obtain will be overestimates on the actual temperature rise.

The governing equations are solved using initial values and boundary conditions, employing the FEM method with adaptive mesh refinement. The convergence study involves two critical points: (i) the delta energy, which represents the change in the S parameter amplitude before and after each mesh refinement and (ii) the stability of physical quantities with respect to mesh refinement. After several iterations, once the criteria of delta energy are met and the key physical quantities remain stable with variations maintained below 1%, the simulation concludes, yielding accurate results.

2.3. Frequency selection

Given the significant loss in biological tissues and the frequency-dependent nature relative permittivity (ε_r), relative permeability (μ_r), and conductivity (σ) of head tissues, selecting an appropriate operating frequency is crucial. To investigate the dependence of focal quality on the excitation frequency, we use a simplified radially symmetric human head model which allows us to obtain a clear insight on focal quality. Trends observed in this section should translate, with slight variations, onto the realistic head model introduced in the previous section. The simplified four-layer spherical human head model, consisting of scalp (3 mm), skull (6 mm), (CSF, 3 mm), and brain matter (146 mm in diameter), is depicted in figures 2(a) and (b). To investigate the penetration depth of microwave signals at different frequencies, we simulate the EM field distribution resulting from a dipole antenna aligned along the z-direction, positioned at $(0, -120, 0)$ mm, as shown in figure 2(a). We compare the E-field intensity along the observation line of the spherical head model at 0.5 GHz, 1.5 GHz, and 2.5 GHz. Figures 2(c)–(e) present the normalized complex E-field magnitude distribution on the axial cross-section at these frequencies, respectively, revealing a declining trend in penetration depth.

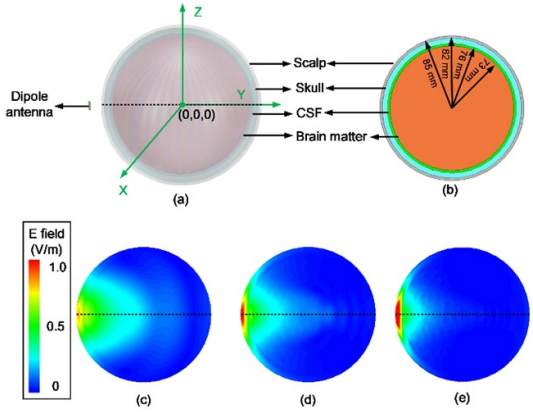

Figure 2. (a) Diagram of the spherical head model. The center of the sphere is (0, 0, 0). A dipole antenna in the z-axis is placed at (0, −120, 0) mm. (b) A cross-section of the sphere head model. (c)–(e) The normalized E-field distributions on the XOY cross-section when the dipole radiates at (c) 0.5 GHz, (d) 1.5 GHz and (e) 2.5 GHz.

Figure 3 illustrates the E-field intensity along the observation line (depicted in figures 2(a), (c)–(e)) at 0.5 GHz, 1.5 GHz, and 2.5 GHz. At a penetration depth of 25 mm along the observation line on the XOY cross-section, the E-field intensities are attenuated by 26.2%, 52.9%, and 62.2%, respectively. We then replicate the dipole 16 times at 22.5° intervals around the z-axis, as shown in figure 4(a), to generate a focal spot in the deep brain region. We observe the focal spot size at different frequencies. Figures 4(b)–(d) show that higher frequencies yield smaller focus sizes. Figure 4(e) compares the normalized E-field profiles along the observation line shown in figure 4(a), showing that the normalized half-width half-maximum E-field values are 0.47 mm, 0.15 mm, and 0.10 mm at 0.5 GHz, 1.5 GHz, and 2.5 GHz, respectively. This indicates that higher frequencies can improve resolution at the cost of focus intensity. Based on the results shown in figure 4, we select 1.5 GHz to obtain a good trade-off balance between resolution and penetration depth. We list the characterized properties at 1.5 GHz for the head tissues in table 1.

[51] reported that the impact of microwave signals on neural activity is negligible at moderate field strengths, even when the field strength reaches up to 230 V m^{-1}. Furthermore [52, 53], demonstrated that exposure to microwave radiation did not impair the rats' ability to learn spatial memory tasks, which indicates that GHz signals have a negligible effect on brain activity. However, some studies have reported that higher carrier frequencies may affect the neuron

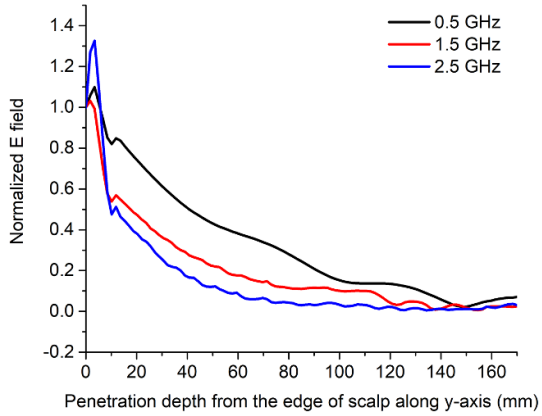

Figure 3. Electric field penetration along the observation line at 0.5 GHz, 1.5 GHz, and 2.5 GHz, respectively. Here 0 mm indicates the edge of the scalp.

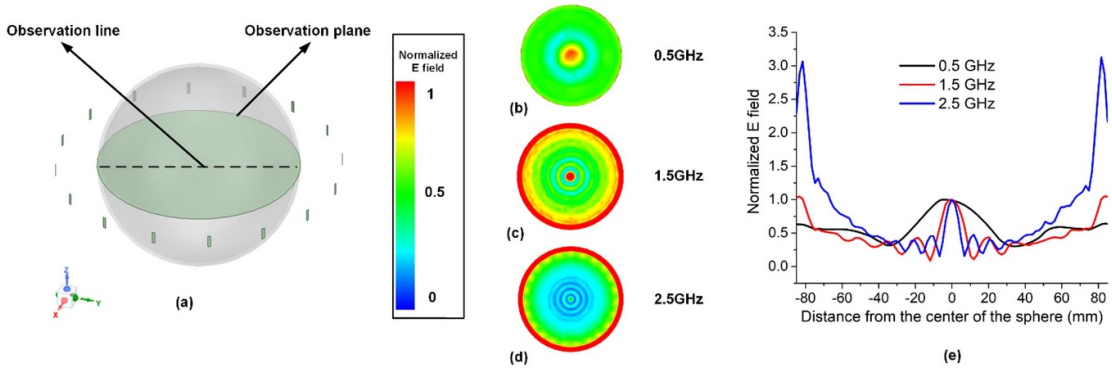

Figure 4. (a) Diagram of the four-layer head model with 16 antennas. (b)–(d) The normalized *E*-field distributions at the observation (*XOY*) plane for (b) 0.5 GHz, (c) 1.5 GHz and (d) 2.5 GHz. (e) Normalized *E*-field distributions at the observation line for 0.5 GHz, 1.5 GHz and 2.5 GHz.

Table 1. Characterized properties of head tissues at 1.5 GHz [58].

	Relative permittivity ε_r	Relative permeability μ_r	Electrical conductivity σ (S m^{-1})	Density ρ (kg m^{-3})	Thermal conductivity k (W/(m·K))	Heat capacity C (J/(kg·K))
White matter	37.50	1.00	0.80	1041.00	0.48	3583.00
Cerebellum	46.90	1.00	1.55	1045.00	0.51	3653.00
Grey matter	50.70	1.00	1.23	1045.00	0.55	3696.00
CSF	67.60	1.00	2.72	1007.00	0.57	4096.00
Skull	19.80	1.00	0.50	1908.00	0.31	1313.00
Muscle	54.00	1.00	1.19	1090.00	0.49	3421.00
Fat	11.10	1.00	0.16	911.00	0.21	3391.00
Eye	68.70	1.00	1.87	1005.00	0.59	4047.00
Skin	39.40	1.00	1.07	1109.00	0.37	3391.00

modulation [19, 54]. Additionally, higher carrier frequencies create a barrier to envelope penetration into deeper brain structures, which will reduce stimulation efficiency. More power is deposited in the superficial regions of the head [55], leading to higher SAR limits and increased temperature compared to cases with lower carrier frequencies. In conclusion, neuronal activity primarily follows the envelope signal and the impact of the 1.5 GHz carrier frequency on neuronal activity must not be overlooked during the treatment.

2.4. Safety analysis

In addition to penetration depth, safety is a critical consideration for deep brain stimulation. Two important quantities of relevance in safety analysis are the SAR [56, 57] and the temperature change due to the EM field. According to [26, 39–43], if the induced

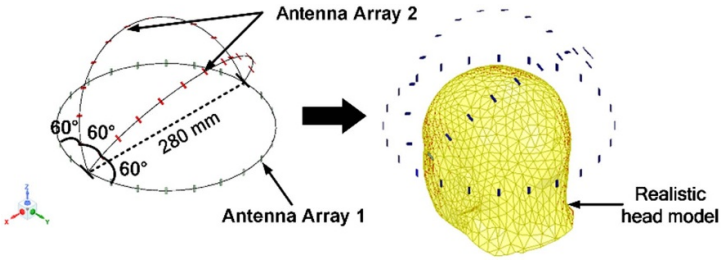

Figure 5. Diagram of the distribution of dipole antennas around the realistic head model. The green-marked elements constitute Antenna Array 1, while the red-marked elements form Antenna Array 2. These arrays are strategically positioned around the head model to illuminate it with electromagnetic waves.

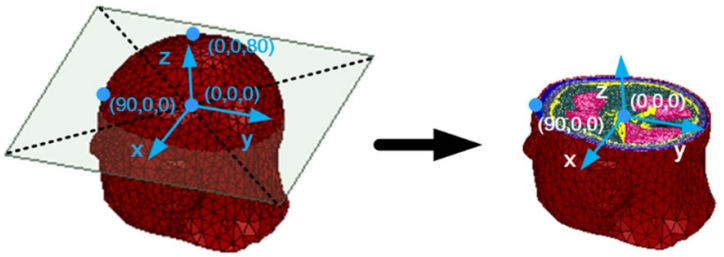

Figure 6. Diagram of the Cartesian coordinate system for the head model. The origin point is positioned 90 mm from the forehead and 80 mm from the top of the head model.

temperature rise is controlled to be less than 1 °C and the SAR value is kept below 10 W kg^{-1}, the proposed frequency is not anticipated to compromise patient safety or comfort.

2.5. Focality in the deep brain and steerability of E-field direction

In the HFSS simulation setup, we position two dipole antenna arrays around the realistic head model, as illustrated in figure 5. Antenna Array 1, depicted in green in figure 5, consists of 24 dipoles equi-spaced in a circular orbit about the head with a diameter of 280 mm on the *xy*-plane. Antenna Array 2, depicted in red in figure 5, consists of 22 dipoles distributed across two semicircular orbits about the head with the same center and diameter as Antenna Array 1, at planes which are 60° rotated from each other and from the *xy*-plane. The realistic head model is placed at the center of the antenna arrays. The origin is 80 mm away from the top of the head model and 90 mm away from the front end of the forehead, as shown in figure 6.

Since the total *E*-field can be calculated by the superposition of the *E*-fields generated by each individual antenna, we express the *E*-field at a certain point $\boldsymbol{r}$ as follows

$$\boldsymbol{E}(\boldsymbol{r}) = \sum_{i=1}^{46} \boldsymbol{E_i}(\boldsymbol{r}), \tag{5}$$

where $\boldsymbol{E}(\boldsymbol{r})$ is the synthesized vector *E*-field at $\boldsymbol{r}$, $\boldsymbol{E_i}(\boldsymbol{r})$ is the *E*-field at $\boldsymbol{r}$ generated by single antenna *i*. In the material property setup, we assume that the head tissues have linear material properties, which means the amplitude and phase of the EM fields at the target point are the vectorial superposition of EM fields of the individual signal sources. Due to the varying distances between each antenna and the target point, as well as the inhomogeneous geometry, the path length varies, resulting in different attenuation factors represented by $A_i(\boldsymbol{r})$. The linear relationship can be mathematically described as

$$\begin{cases} |\boldsymbol{E_i}(\boldsymbol{r})| = A_i(\boldsymbol{r}) \cdot P_i(\boldsymbol{r}) \\ \angle \boldsymbol{E_i}(\boldsymbol{r}) = B_i(\boldsymbol{r}) + \angle \mathrm{Ant}_i(\boldsymbol{r}) \end{cases}, \tag{6}$$

where $A_i(\boldsymbol{r})$ is the coefficient between the amplitude of *E*-field from antenna *i* and the power $P_i(\boldsymbol{r})$ radiated from antenna i; $\angle \boldsymbol{E_i}(\boldsymbol{r})$ is the phase of $\boldsymbol{E_i}(\boldsymbol{r})$; $\angle \mathrm{Ant}_i$ is the excitation phase of *i*th antenna; $B_i(\mathbf{r})$ is the phase difference between the phase of *E*-field at $\boldsymbol{r}$ from antenna *i* and the excitation phase of antenna *i*.

We first excite the dipole antennas one by one to observe $\angle \boldsymbol{E_i}(\boldsymbol{r})$ and then tune the $\angle \mathrm{Ant}_i(\boldsymbol{r})$ to make each $\angle \boldsymbol{E_i}(\boldsymbol{r}) = 0$, which leads to constructive interference of $\boldsymbol{E}(\boldsymbol{r})$, hence maximizing it at the desired location $\boldsymbol{r} = \boldsymbol{r}_0$. Figure 7 illustrates the process.

In addition to generating a focality inside the brain model, we also demonstrate the steerability of the *E*-field direction. Antenna Array 1 and Antenna Array 2 both contribute to $\boldsymbol{E}(\boldsymbol{r})$, where Antenna Array 1 generates the *z*-directed component of $\boldsymbol{E}(\boldsymbol{r})$ and Antenna Array 2 generates the *y*-directed component of $\boldsymbol{E}(\boldsymbol{r})$. The *x*-directed *E*-field is not generated in this work: if needed, one can superimpose an Antenna Array 3 90° rotated from Antenna Array 2

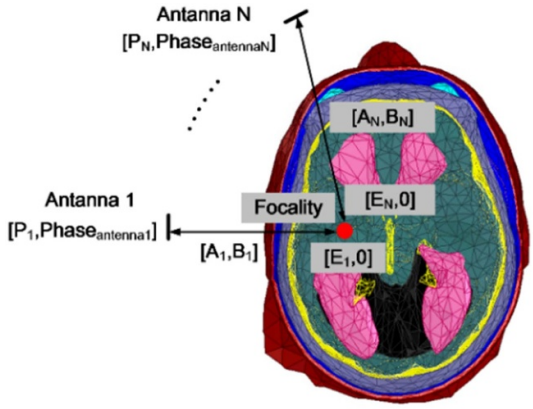

Figure 7. Diagram of tuning and getting a focality. $\text{Phase}_{\text{antenna1}-\text{N}}$ are tuned so that $\text{Phase}_{1-\text{N}}$ are all equal to 0.

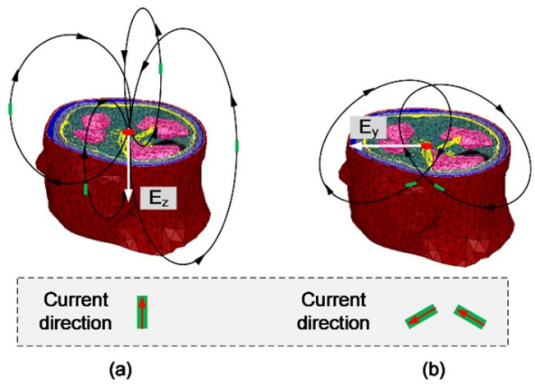

Figure 8. Mechanism of *E*-field steerability. Antenna Array 1 and antenna Array 2 generate *z*-direction and *y*-direction *E*-field components, respectively. The total *E*-field is the synthesis of the two components.

along the *z*-axis to also generate an *x*-directed *E*-field. Alternatively, one can rotate Antenna Array 2 along the *z*-axis to control the *E*-field direction along the *x*- and *y*-directions. As shown in figure 8(a), elements from Antenna Array 1 generate a synthesized *E*-field at a certain point. Since the dipoles are all vertical, the synthesized *E*-field is mostly in the *z*-direction. Figure 8(b) illustrates the EM effect of Antenna Array 2. The elements from Antenna Array 2 are excited with current in mirror symmetry but with opposite directions, which cancels out the *z*-directed and *x*-directed *E*-field components and enhances the *y*-direction *E*-field component. Due to the inhomogeneous property of the 3D realistic human head model, an *x*-directed *E*-field exists but it is much weaker than E_y and E_z. Therefore, we consider the total *E*-field to be synthesized by E_y and E_z. With these two directional *E*-field components, we can control the direction of the *E*-field by adjusting the power strength of the antenna arrays.

In practical case, the system consists of several main components, as shown in figure 9, including a 1.5 GHz voltage-controlled oscillator (VCO), a 10 Hz modulation switch, a power monitor, a field-programmable gate array (FPGA), multiple phase shifters, several amplifiers and a helmet with the antenna array elements mounted on it. The signals are managed by an FPGA, with phase alignment achieved through phase shifters and antenna weighting accomplished via amplifiers. The hardware mentioned in [59] can be developed to generate GHz signals with a 150 Hz frequency resolution. The 10 Hz envelope can then be generated using a modulated switch [25], ensuring that both the envelope and the carrier signals can be generated with sufficiently high precision.

3. Simulation results

In this section, we report full-wave simulation results of *E*-field focality in the deep brain region with steerable directionality at 1.5 GHz using a realistic 3D head model. Additionally, using a multi-physics simulation, we study the temperature and SAR distribution within the head model during the stimulation process.

3.1. Focality of E-field

To demonstrate the focality of the *E*-field in the deep brain region, we select 3 target focal locations—(0, 0, 0) mm, (−10, 0, 10) mm, and (20, 20, 0) mm—to showcase the feasibility of the proposed method. We designate these focalities as Case I, Case II, and Case III, respectively. Based on previous research [31, 32], 40 V m^{-1} extracellular *E*-field excitation with a 10 Hz envelope can induce neuronal spiking. Therefore, we generate *E*-field focalities with intensities of 40 V m^{-1} (16 V m^{-1} in the *y* direction and 36.7 V m^{-1} in the *z* direction) at these three locations. Figures 10(a)–(c) show the successful generation of *E*-field focuses on the three locations.

Following [45], we use an *E*-field threshold at 75% of the maximum *E*-field as the cut-off contour to analyze the size of the focal region. That is to say, we calculate the area of the region with $|\boldsymbol{E}| \geqslant 30$ V m^{-1}. The simulated complex magnitude of the *E*-field, in (E_x, E_y, E_z) are (2.3, 15.8, 36.6) V m^{-1}, (3.7, 15.7, 36.7) V m^{-1}, and (5.1, 15.7, 36.4) V m^{-1}, in Cases I to III respectively. As expected, most of the power is attenuated in the superficial region, as shown in figures 10(a)–(c). However, sufficient power can still be delivered into the brain and generate a focality. At the three targeted points, *E*-fields of 40 V m^{-1}, lying mostly on the *yz*-plane, are generated. The *x*-directed *E*-field increases slightly as we move towards the cortical region. This phenomenon arises due to the uneven phase distribution especially in the superficial region, resulting in an unwanted *x*-component of *E*-field. However, in the deep brain region, the phase difference of *E*-fields from extracellular excitations is minimal, which accounts for the higher purity of the *E*-field as the focus is generated deeper into the brain. In summary, it is indeed feasible to deliver

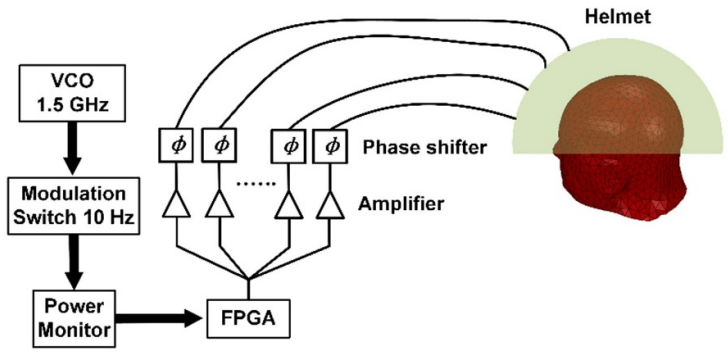

Figure 9. Schematic diagram of the proposed system. The carrier frequency is generated by a 1.5 GHz voltage-controlled oscillator (VCO). The microwave signal is then modulated using a 10 Hz modulation switch, and the modulated signal is delivered to a power monitor to track the power level. A field-programmable gate array (FPGA) is employed to calculate the appropriate phase and amplitude for each antenna element. Phase alignment and amplitude weighting are achieved through the use of phase shifters and amplifiers. The output signals are transmitted to the helmet for illumination treatment.

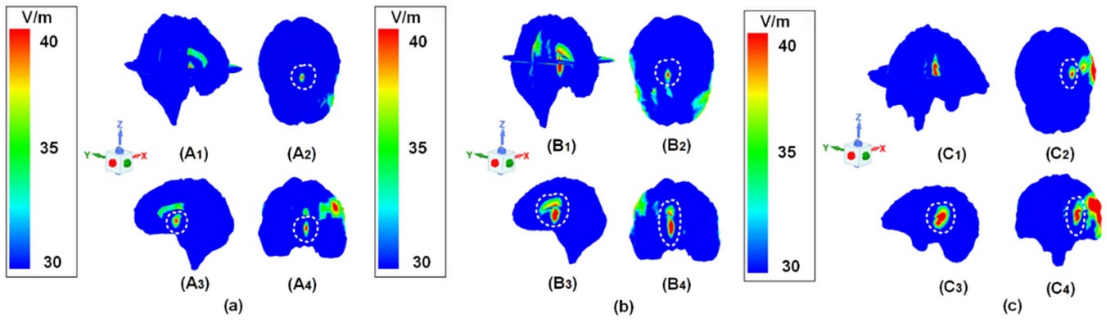

Figure 10. Focality generation at (a) Case I (0 mm, 0 mm, 0 mm), (b) Case II (−10 mm, 0 mm, 10 mm) and (c) Case III (20 mm, 20 mm, 0 mm). The focalities are circled in white dashed lines. Panels (A, B, C)$_{2-4}$ show the distribution of *E*-field magnitude on the *XOY, YOZ* and *XOZ* planes, respectively. The superficial region of the head model has been masked, and the *E*-field is plotted exclusively within the brain volume to clearly illustrate the focality in the deep regions.

Table 2. Size of focality of each case at different cross-sections.

	Case I	Case II	Case III
Focality at *XOY* (mm^2)	72.5	148.0	176.0
Focality at *XOZ* (mm^2)	118.0	348.0	368.5
Focality at *YOZ* (mm^2)	244.5	958.0	676.5

high-frequency EM fields into the deep brain region to generate a focal spot.

Table 2 shows the size of the focality for each case at *XOY, XOZ*, and *YOZ* cross-sections, respectively. When the focus is generated at the deep region of the brain (Case I), the cross-sectional areas of the focality at the *XOY, XOZ*, and *YOZ* planes are 72.5 mm^2, 118.0 mm^2, and 244.5 mm^2, respectively. As the focality is shifted to (−10, 0, 10) mm (Case II), its size gets larger compared to the focality at the original point, but is still relatively small, with cross-sectional areas of 148.0 mm^2, 348.0 mm^2 and 958.0 mm^2 at the *XOY, XOZ* and *YOZ* planes respectively. The focality of Case III is the largest, with 176.0 mm^2, 368.5 mm^2 and 676.5 mm^2 at the *XOY, XOZ* and *YOZ* planes respectively. As it is farther from the hippocampus, the area of the *XOZ* cross section is slightly smaller than in Case II.

Table 3 presents the comparison of the area ratio, simulation depth, carrier frequency, beating frequency and applied model between the proposed work and a few previous works. The TIS method is used in research [18, 33–37], with kHz carrier frequency wave and 10 Hz envelop signal. The area ratio, defined as the ratio of focality to the corresponding cross-sectional area, indicates that the previously reported ratios (ranging from 2.17% to 33.4%) are significantly higher than our findings. Besides, as the complexity of the applied head model increases, the ratio also exhibits a greater proportion. All studies in this context focus on deep regions within the model, implying that for a typical-sized head model, the penetration depth is approximately 10 cm. Song *et al* [33] applies a circle with a 1 m radius as the model in a 2D analysis and hasn't given the penetration depth. Grossman *et al* [18] applies a spherical head model with a radius of 5 cm. In conclusion, the usage of a 1.5 GHz carrier frequency has led to (i) the generation of a much smaller focality [18, 33–37], and

Table 3. Comparison between the proposed work and a few previous works.

	Area Ratio	Stimulation depth	Carrier frequency	Beating frequency	Applied model
The proposed Work	*XOY*: 0.34% *YOZ* :0.37% *XOZ*: 0.97%	∼100 mm	1.5 GHz	10 Hz	9 tissue 3D realistic model
[33]	*XOY*: 2.17%	/	2 kHz	10 Hz	2D circle
[18]	*XOY*: 15.04%	∼50 mm	2 kHz	10 Hz	4-layer sphere
[34]	*XOY*: 33.36%	∼100 mm	2 kHz	10 Hz	9 tissue 3D realistic model
[35]	*XOZ*: 10.59%	∼100 mm	2 kHz	10 Hz	9 tissue 3D realistic model
[36]	*XOY*: 9.94%	∼100 mm	1 kHz&10 kHz	10 Hz	4 tissue 3D realistic model
[37]	*YOZ*: 11.01%	∼100 mm	2 kHz	10 Hz	5 tissue 3D realistic model

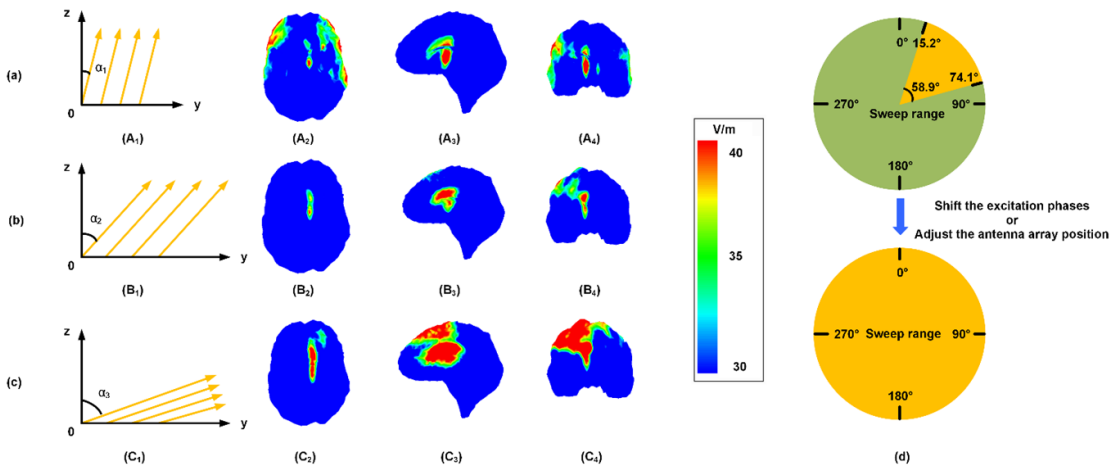

Figure 11. Illustration of the *E*-field steerability at the observation point (−10, 0, 10) with angles: (a) $\alpha_1 = 15.2°$; (b) $\alpha_2 = 45°$; (c) $\alpha_3 = 74.1°$. Panels (A_1, B_1, C_1) depict the *E*-field directionality at the focal point on *YOZ* plane. Panels (A, B, C)$_{2-4}$ show the complex magnitude of the *E*-field distribution across the *XOY, YOZ*, and *XOZ* cross sections, respectively. The fan chart (d) demonstrates the sweep angle range achievable with the current antenna arrays (top). By shifting the excitation phases and adjusting the antenna array positions, a 360° scanning of the *E*-field at the focal point can be achieved. The superficial region of the head model has been masked, and the *E*-field is plotted exclusively within the brain volume to clearly illustrate the focality in the deep regions.

(ii) the elimination of hot spots in spurious regions [37]. This demonstrates that using higher working frequency can improve the focal size and purity and thereby enhance the accuracy of stimulation.

3.2. Steerability of the E-field direction

Since the target *E*-field is synthesized by E_y and E_z, we can adjust the direction of the *E*-field by changing the ratio between E_y and E_z. In this section, Case II is used as an example for the demonstration. As shown in figures 11(A_1), (B_1) and (C_1) by changing the relative excitation weights for Antenna Array 1 and Antenna Array 2, we achieve focalities with *E*-fields which are directed at $\alpha_1 = 15.2°$,*E*-field $\alpha_2 = 45.0°$ *E*-field and $\alpha_3 = 74.1°$ as measured from the $+z$-axis. The complex magnitude of the *E*-field for the three cases is (4.3, 10.4, 39.6) V m^{-1}, (2.4, 28.2, 28.4) V m^{-1}, and (1.9, 39.7, 10.9) V m^{-1}, respectively. In all three cases, very week *x*-directed *E*-fields are generated, indicating that the *E*-field still mostly lies on the *yz*-plane. Small direction impurities limit the range of direction adjustment to about 60° (per quadrant). While we demonstrate *E*-field direction steerability over the first quadrant, by shifting the excitation phases of Antenna Arrays 1 and 2 by 180°, we can achieve the same steerability over the second, third and fourth quadrants. To access the remaining angular regions, a slight physical rotation of the antenna arrays can be employed, thereby enabling full directional coverage. Figure 11(d) gives a graphical summary of it. Figures 11(A2)–(C4) show the distribution of the complex magnitude of the *E*-field at the

Table 4. Size of focality of each case at different cross-sections.

	Steerable angle = 15.2°	Steerable angle = 45°	Steerable angle = 74.1°
Focality at *XOY* (mm^2)	294.0 (1.4%)	293.0 (1.4%)	766.0 (3.6%)
Focality at *YOZ* (mm^2)	1020.0 (3.2%)	1238.0 (3.9%)	2550.0 (8.0%)
Focality at *XOZ* (mm^2)	406.0 (1.6%)	428.0 (1.7%)	524.0 (2.1%)

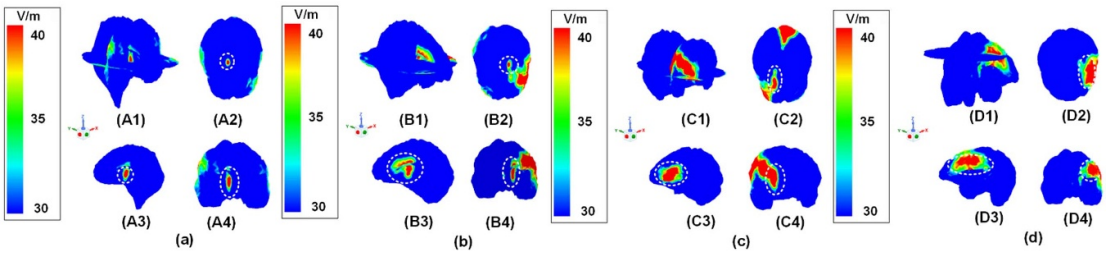

Figure 12. Focality generation at (a) (−10 mm,0 mm, 0 mm), (b) Case II (10 mm, 0 mm, 10 mm), (c) Case III (−20 mm, −20 mm, 0 mm) and (d) (30 mm, 0, 30 mm). The focalities are circled in white dashed lines. Panels (A, B, C)$_{2-4}$ show the distribution of *E*-field magnitude on the *XOY, YOZ* and *XOZ* planes, respectively. The superficial region of the head model has been masked, and the *E*-field is plotted exclusively within the brain volume to clearly illustrate the focality in the deep regions.

three cross-sections. As α approaches 90°, the shape of the focality changes and its size slightly increases, but the target point is still covered by the designed *E*-field. In conclusion, by adjusting the relative input power strengths to the antenna arrays, we can generate an *E*-field focality to a wide-range of locations and, at the same time, control the direction of the *E*-field. This can effectively stimulate the desired neural activity and minimize unnecessary EM field exposure to the patient.

The focal spot dimensions at angles of 15.2°, 45°, and 74.1° on the *XOY, YOZ*, and *XOZ* planes are summarized in table 4. The area ratios between the focality and the corresponding cross section are shown in the brackets. The results indicate that the focal quality degrades with increasing angle; however, we can maintain an *E*-field strength of 40 V m^{-1} at the focus point by adjusting the input power to the antennas. Furthermore, although the focal quality diminishes at larger angles, the focal spot size remains smaller compared to those observed in comparable studies employing kHz-frequency carriers in table 3. The adjustment of focus can be achieved at any position within the brain. We provide four additional focal points as shown in figure 12. As demonstrated in figure 12, focal points are generated at coordinates (−10 mm, 0, 0), (10 mm, 0, 10 mm), (−20 mm, −20 mm, 0), and (30 mm, 0, 30 mm). Consistent with the conclusion in the paper, the spatial resolution of the focal points is reduced at the cortical region due to an uneven phase distribution.

3.3. Temperature distribution and SAR distribution

For the investigation of temperature distribution in the head model, we excite the head model with TI signals at 1.5 GHz with a 10 Hz envelope. The TI signal is operated for 2 s and repeated every 4 s, which means the duty cycle is 50%. The excitation current for each Antenna *i*, $f_i(t)$, is shown in (7),

$$f_i(t) = A_i \sin(\omega_0 t) \cos(\omega_b t)\, s(t) \tag{7}$$

where A_i is the complex amplitude achieved from (4) for each antenna, $\omega_0 = 2\pi \cdot 1.5$ GHz is the carrier angular frequency, $\omega_b = 2\pi \cdot 10$ Hz is the beat frequency, and

$$s(t) = \begin{cases} 2, & 0 \leqslant t < 2\ s \\ 0, & 2s \leqslant t \leqslant 4\ s \end{cases} \tag{8}$$

is the temporal pulse. In this section, COMSOL Multiphysics, a commercial Multiphysics co-simulation software, is utilized to obtain the temperature and SAR within the human head, when the setup is used to generate a desired focality within the head. By assigning the designed complex amplitudes for each excitation, the temperature distribution for the three cases can be visualized in figures 13–15. From sub-figures (a)–(c) in figures 13–15, it is evident that the temperature rises as the duration of illumination increases. When the excitation time is short, for example, 10 min as shown in figures 13–15(a), the temperature increase is negligible. Table 3 shows that,

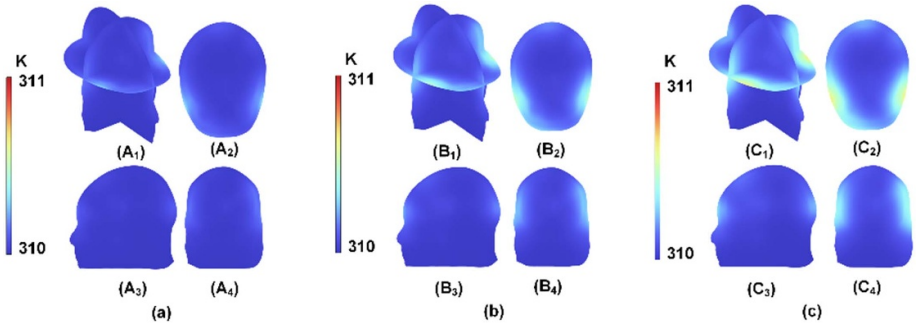

Figure 13. Temperature distribution in the realistic head model of Case I (focality is at (0,0,0) mm) at (a) $t = 10$ min, (b) $t = 20$ min and (c) $t = 30$ min. Panels (A, B, C)$_{2\text{-}4}$ show the distribution of temperature on the *XOY, YOZ* and *XOZ* plane, respectively.

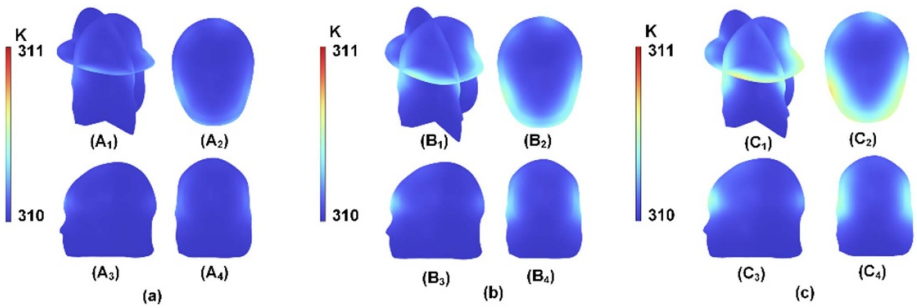

Figure 14. Temperature distribution in the realistic head model of Case II (focality is at (−10,0,10) mm) at (a) $t = 10$ min, (b) $t = 20$ min, and (c) $t = 30$ min. Panels (A, B, C)$_{2\text{-}4}$ show the distribution of temperature on the *XOY, YOZ* and *XOZ* plane, respectively.

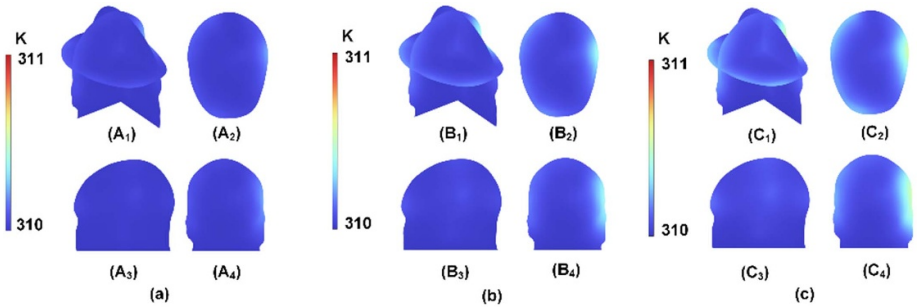

Figure 15. Temperature distribution in the realistic head model of Case III (focality is at (20, 20, 0) mm) at (a) $t = 10$ min, (b) $t = 20$ min and (c) $t = 30$ min. Panels (A, B, C)$_{2\text{–}4}$ show the distribution of temperature on the *XOY, YOZ* and *XOZ* plane, respectively.

at 10 min, there is a temperature increase of approximately 0.2–0.3 K at the edge of the head model. After 20 min, the temperature increases by 0.50 K, 0.58 K, and 0.41 K for Case I, Case II, and Case III, respectively, which falls within the safety range of temperature increase (1 K). Continuing to illuminate the head model for 30 min, the temperature can reach up to 310.76 K as depicted in in figures 13–15(c) and table 5, which is close to the upper limit of temperature safety. Overall, the temperature increase is acceptable for both instant brain stimulation and chronic brain stimulation

We have also examined the distribution of SAR within the brain model. Figures 16(a)–(c) illustrate the SAR_{10g} distribution within the brain model, and table 3 provides the maximum SAR_{10g} values for the three cases. By employing our method to generate a focal region that achieves the required strength for neuronal excitation, the SAR_{10g} remains below 3.0 W kg^{-1}, which is lower than the IEC SAR local

Table 5. Maximum temperature and SAR_{10g} for 3 cases.

	Case I	Case II	Case III
Maximum temperature at $t = 10$ min (K)	310.30	310.35	310.23
Maximum temperature at $t = 20$ min (K)	310.50	310.58	310.41
Maximum temperature at $t = 30$ min (K)	310.64	310.76	310.56
Maximum SAR_{10g} (W kg^{-1})	2.39	1.71	1.12
Maximum SAR_{1g} (W kg^{-1})	2.70	1.86	1.52

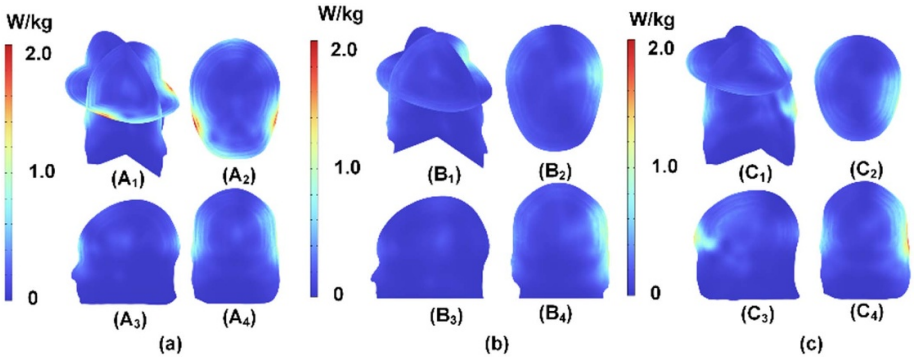

Figure 16. SAR_{10g} distribution in the realistic head model of (a) Case I; (b) Case II; (c) Case III. Panels $(A, B, C)_{2-4}$ show the distribution of SAR_{10g} on the *XOY, YOZ* and *XOZ* plane, respectively.

head SAR_{10g} criteria of 10 W kg^{-1} [26]. Table 5 also includes the SAR_{1g} values obtained from the simulation results, which are higher than the corresponding SAR_{10g} values but still much lower than the IEC head SAR_{10g} criteria.

[60] mentioned that the mean value of the local cooling rate of the human head is within the range of 0.07 ± 0.04 °C min^{-1}. Additionally [61], reported that with the use of cooling techniques, the most rapid cooling rate observed is 0.35 °C min^{-1}. In conclusion, the cooling time can be effectively managed to ensure that the patient's head temperature returns to normal before the next treatment session.

4. Discussion

In this paper, we introduce a novel approach for NDBS utilizing a 1.5 GHz microwave signal modulated at 10 Hz. We validate this method using a realistic 3D human head model. Our simulation results demonstrate that the proposed method achieves drastically higher spatial resolution with reduced input power while maintaining delivered power within a safe range compared to previous works. In the following section, we discuss several key aspects of our work that guarantee further consideration to enhance its comprehensiveness and robustness.

4.1. Focality resolution as a function of position

As detailed in section 3.1, in the deep brain region, the phase difference of *E*-fields from extracellular excitations is minimal, contributing to the higher purity of the *E*-field as the focus penetrates deeper into the brain. However, the *x*-directed *E*-field intensifies as we approach the cortical region, leading to a slightly reduced resolution near the brain's superficial region. This phenomenon is attributed to the uneven phase distribution, particularly in the superficial region, which results in an undesired *x*-component of the *E*-field. Several algorithms have been reported to (i) maximize the *E*-field strength at the target region, (ii) minimize surrounding hotspots, and (iii) enhance the resolution of the focality, including adaptive feedback algorithms [62], genetic algorithms [63], and deep learning algorithms [64], etc. In future studies, incorporating these algorithms could enhance spatial resolution near the cortical region. While the simple methodology used in this paper achieves high spatial resolution in deeper brain region, which is

of primary interest for NDBS, the aforementioned methods can be used to improve the focality size beyond that demonstrated in this paper in the superficial region.

4.2. Excitation of hotspots near the skull

In some simulations we have observed the excitement of hotspots near the skull. Hotspots are present near the skull and CSF boundary due to differences in (i) tissue properties, such as thermal conductivity and specific heat capacity, and (ii) anatomical boundaries, with the skull acting as a heat barrier due to its higher density. Simulation results confirm that the SAR values and temperatures are significantly higher in the superficial region of the head model, as illustrated in figures 13–16, compared to the brain matter region. Notwithstanding, we have shown in table 5 that a sufficiently strong *E*-field can be excited at the desired focal location while the maximum SAR and temperature change fall within the commonly accepted safety levels. In the future, adaptive control systems and optimization algorithms for energy delivery could be employed to address the heterogeneity of heating.

4.3. Effects of the EM field outside the target region

By applying controlled *E*-fields to specific neuroanatomical landmarks using the TIS method, we achieve neuron activation through action potential initiation [12] in the target area. This offers promising therapeutic potential for treating diseases associated with neuronal dysfunction and may pave the way for non-invasive neuromodulation-based treatments [65, 66]. In brain regions outside the target area, neurons are also influenced by the applied *E*-field. Nevertheless, as the *E*-field strength is maintained below the activation threshold, no action potentials are triggered. Notwithstanding the above, the stimulation we apply may inadvertently affect the local field potential (LFP) in a region outside the targeted area, modulating the collective activity of a population of neurons and potentially enhancing overall neuronal excitability and synaptic interactions [67]. It is yet unknown whether our proposed waveform (a microwave *E*-field modulated at a low-frequency envelope) will affect the LFP. In any case, we note that neural modulation effects stemming from a change in the LFP, are normally much weaker than that achieved by TIS.

4.4. Power budget for the system

The input power level is a critical factor in ensuring the efficacy of the proposed system. As illustrated in figure 17, two spherical surfaces are constructed around the head model to evaluate the Poynting vector flux: Sphere 1 encloses only the head model, while Sphere 2 encompasses both the antenna arrays and head model. As detailed in section 3.1, the *E*-field strength at the target point is 40 V m^{-1}. Under this specified field strength standard, the EM power flowing into Sphere 1 is 0.9 W, which means the head absorbs the power of 0.9 W. A total radiated power of 4.8 W from all antennas, which accounts for the impedance mismatch reflections and field interferences among antennas in the array, can be obtained by integrating the Poynting vector over the Sphere 2. In future work, our focus will be on three key areas: (i) optimizing the mutual coupling of antenna array elements within a narrow frequency band to enhance efficiency; (ii) achieving impedance matching through the use of index-matching gels to minimize reflections and maximize power transfer; and (iii) designing unidirectional antennas to ensure that the majority of radiated power is directed towards the head, thereby improving system performance. In general, the radiated power budget from the current system is calculated to be 4.8 W and by engineering the antenna pattern and optimizing impedance matching to the head, one can lower the required power from 4.8 W to a value much closer to 0.9 W.

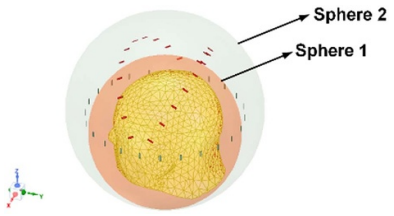

Figure 17. Antenna arrays with two spherical surfaces for the integration of Poynting vector. The spheres are built as non-model objects for the sole purpose of calculating power flows, which means they do not affect the distribution of fields.

4.5. Design of antenna arrays

The design of antenna arrays will be a critical factor for the system. In practical applications, we will employ antennas with a high front-to-back (F/B) ratio, such as patch antennas, to effectively illuminate the head model. To position the antennas at the desired locations, we can utilize 3D printing technology to fabricate a customized helmet structure (as illustrated in [68]), onto which the antennas can be mounted. Currently, we have not yet optimized the antenna configuration. However, we believe it is feasible to reduce the number of antennas with minimal impact on localization. To demonstrate this, we decrease the number of antennas in Antenna Array 1 from 24 to 12 and in Antenna Array 2 from 22 to 11. Simultaneously, we maintain the E_y and E_z field strengths at the same levels as in Case I (3.5, 15.7, 36.5 V m^{-1}). The results indicate that the focus area of the modified Case I is slightly larger than that of the original case (8.3%, 3.7%, and 5.7% for the *XOY, YOZ*, and *XOZ* planes, respectively), but the values remain comparable. This suggests that in future research, when constructing the helmet to house the

antennas, we can reduce the number of elements while preserving performance.

4.6. Interference between the proposed work and wireless devices

The carrier frequency of 1.5 GHz is close to the operating frequencies of typical mobile devices, which could potentially lead to EM interference between this stimulation system and such devices. However, due to the significant frequency difference between our proposed system and those commonly used in mobile devices [69, 70], along with the relatively low *E*-field strength emitted by these devices [71–73], the likelihood of interference between mobile device signals and our equipment is minimal.

4.7. Computational considerations

Currently, on a simulation server equipped with an Intel(R) Xeon(R) Platinum 8160 CPU @ 2.10 GHz and 256 GB of memory. All necessary information regarding the antenna array elements is collected prior to treatment, enabling real-time deployment with the current setup. Future hardware and computation improvements will lend support to investigations on real-time optimizations of the excitation weights, data monitoring, and signal adaptation. Overall, there is significant potential for real-time clinical use of the proposed system, given that the relevant information is established before treatment with acceptable computation cost.

4.8. Future work

In the next phase of our research, we will focus on designing the helmet structure to which microwave antennas will be integrated. Upon completing this helmet prototype, we will proceed with experimental experiments, including studies on human head-phantoms, animal models, and eventually human subjects. Following validation in animal experiments, we aim to transition this device into clinical applications, targeting improved focus resolution and reduced power requirements compared to existing technologies.

A specific signal highly correlated with certain neurological conditions must be identified prior to clinical applications to serve as the basis for stimulation. The response time of the system will depend on the characteristics of the selected triggering signal. Since numerous studies have demonstrated significant variations in brain morphology and tissue properties due to age [74–76], gender [77–79] and pathological conditions [68, 80, 81]. These variations result in highly individualized EM field distributions within the brain. To translate the proposed method into clinical application, it is necessary to perform a pre-treatment MRI scan of the patient's brain to guide the customization of the excitation amplitude and phase of the antenna array [75]. Alternatively, after extracting the MRI image of the patient's brain and identifying the lesion area, we can initiate stimulation once all preparations are complete.

5. Conclusion

This paper presents a 1.5 GHz non-invasive TIS deep brain stimulation method based on a realistic 3D human head model. Through this method, we have successfully demonstrated the feasibility of focusing on the deep brain region using microwave signals. The subsequent investigation of temperature and SAR further indicates that our method has the potential to deliver the necessary power to the targeted brain region within the safe SAR and temperature range. The focal spot generated by our method is smaller than the previous brain stimulation methods, which apply a kHz signal as the carrier wave. It shows potential for enhancing clinical treatment accuracy in the future. Additionally, we have demonstrated the ability to control the direction of the *E*-field at the focal point. By achieving this steerability, we can lower the *E*-field strength required for neuronal activation and simultaneously minimize the health risk resulting from exposure during treatment. Finally, the focality excitation simulations are performed on a 3D, realistic human head model with full-wave EM and multiphysics simulators, which makes the result meaningful compared to idealized cylindrical and/or spherical phantoms. In conclusion, the non-invasive 1.5 GHz TIS deep brain stimulation technique we have proposed represents an appealing prospect for future deep brain stimulation therapy.

Data availability statement

All data that support the findings of this study are included within the article (and any supplementary files).

Acknowledgment

This work was supported by the Research Grants Council of the Hong Kong SAR, China, under Project AoE/E-101/23-N.

ORCID iDs

Chen Xue 0000-0002-4041-3251
Alex M H Wong 0000-0002-8105-5964

References

[1] Vetkas A *et al* 2022 Deep brain stimulation targets in epilepsy: systematic review and meta-analysis of anterior and centromedian thalamic nuclei and hippocampus *Epilepsia* **63** 513–24
[2] Loddenkemper T, Pan A, Neme S, Baker K B, Rezai A R, Dinner D S, Montgomery E B and Lüders H O 2001 Deep brain stimulation in epilepsy *J. Clin. Neurophysiol.* **18** 514–32
[3] Mahlknecht P, Foltynie T, Limousin P and Poewe W 2022 How does deep brain stimulation change the course of Parkinson's disease? *Mov. Disorders* **37** 1581–92

[4] Hariz M and Blomstedt P 2022 Deep brain stimulation for Parkinson's disease *J. Intern. Med.* **292** 764–78
[5] Vercueil L, Pollak P, Fraix V, Caputo E, Moro E, Benazzouz A, Xie J, Koudsie A and Benabid A-L 2002 Deep brain stimulation in the treatment of severe dystonia *J. Neurol.* **248** 695–700
[6] Vidailhet M *et al* 2013 Deep brain stimulation for dystonia *Handb. Clin. Neurol.* **116** 167–87
[7] Flora E D, Perera C L, Cameron A L and Maddern G J 2010 Deep brain stimulation for essential tremor: a systematic review *Mov. Disorders* **25** 1550–9
[8] Chopra A, Klassen B T and Stead S 2013 Current clinical application of deep-brain stimulation for essential tremor *Neuropsychiatr. Dis. Treat.* **9** 1859–65
[9] Mink J W *et al* 2006 Patient selection and assessment recommendations for deep brain stimulation in Tourette syndrome *Mov. Disorders* **21** 1831–8
[10] Schrock L E *et al* 2015 Tourette syndrome deep brain stimulation: a review and updated recommendations *Mov. Disorders* **30** 448–71
[11] Huang H M, Yang R, Tan Z-H, He H-K, Zhou W, Xiong J and Guo X 2019 Quasi-hodgkin–huxley neurons with leaky integrate-and-fire functions physically realized with memristive devices *Adv. Mater.* **31** 1803849
[12] Mirzakhalili E, Barra B, Capogrosso M and Lempka S F 2020 Biophysics of temporal interference stimulation *Cell Syst.* **11** 557–72
[13] Zhang X, Roppolo J R, de Groat W C and Tai C 2006 Mechanism of nerve conduction block induced by high-frequency biphasic electrical currents *IEEE Trans. Biomed. Eng.* **53** 2445–54
[14] Liu X, Qiu F, Hou L and Wang X 2022 Review of noninvasive or minimally invasive deep brain stimulation *Front. Behav. Neurosci.* **15** 820017
[15] Valero-Cabré A, Amengual J L, Stengel C, Pascual-Leone A and Coubard O A 2017 Transcranial magnetic stimulation in basic and clinical neuroscience: a comprehensive review of fundamental principles and novel insights *Neurosci. Biobehav. Rev.* **83** 381–404
[16] Boes A D, Kelly M S, Trapp N T, Stern A P, Press D Z and Pascual-Leone A 2018 Noninvasive brain stimulation: challenges and opportunities for a new clinical specialty *J. Neuropsychiatry Clin. Neurosci.* **30** 173–9
[17] Palm U *et al* 2016 tDCS for the treatment of depression: a comprehensive review *Eur. Arch. Psychiatry Clin. Neurosci.* **266** 681–94
[18] Grossman N *et al* 2017 Noninvasive deep brain stimulation via temporally interfering electric fields *Cell* **169** 1029–41
[19] Esmaeilpour Z, Kronberg G, Reato D, Parra L C and Bikson M 2021 Temporal interference stimulation targets deep brain regions by modulating neural oscillations *Brain Stimul.* **14** 55–65
[20] Bennett B D 2000 Intrinsic membrane properties underlying spontaneous tonic firing in neostriatal cholinergic interneurons *J. Neurosci.* **20** 8493–503
[21] Khaliq Z M and Raman I M 2006 Relative contributions of axonal and somatic Na channels to action potential initiation in cerebellar Purkinje neurons *J. Neurosci.* **26** 1935–44
[22] Bean B P 2007 The action potential in mammalian central neurons *Nat. Rev. Neurosci.* **8** 451–65
[23] Platkiewicz J and Brette R 2010 A threshold equation for action potential initiation *PLoS Comput. Biol.* **6** e1000850
[24] Ahsan F, Chi T, Cho R, Sheth S A, Goodman W and Aazhang B 2022 EMvelop stimulation: minimally invasive deep brain stimulation using temporally interfering electromagnetic waves *J. Neural Eng.* **19** 046005
[25] Oh S, Jung D, Seo T, Huh Y, Cho J and Oh J 2021 6.5-GHz Brain stimulation system using enhanced probe focusing and switch-driven modulation *IEEE Trans. Microw. Theory Tech.* **69** 4107–17
[26] IEC/IEEE P62209-1528a/D1 2025 *IEC/IEEE International Standard—Measurement Procedure for the Assessment of Specific Absorption Rate of Human Exposure to Radio Frequency Fields from Hand-Held and Body-Mounted Wireless Communication Devices—Part 1528: human Models, Instrumentation, and Procedures (Frequency Range of 4 MHz to 10 GHz) Amendment of IEC/IEEE 62209-1528:2020* (International Electrotechnical Commission (IEC)) pp 1–26
[27] Giles A R 1987 Guidelines for the use of animals in biomedical research *Thromb Haemost* **58** 1078–84
[28] Maiti S, Frielinghaus H, Gräßel D, Dulle M, Axer M and Förster S 2021 Distribution and orientation of nerve fibers and myelin assembly in a brain section retrieved by small-angle neutron scattering *Sci. Rep.* **11** 17306
[29] Chen H I, Jgamadze D, Lim J, Mensah-Brown K, Wolf J A, Mills J A and Smith D H 2019 Functional cortical axon tracts generated from human stem cell-derived neurons *Tissue Eng. A* **25** 736–45
[30] Missey F, Rusina E, Acerbo E, Botzanowski B, Trébuchon A, Bartolomei F, Jirsa V, Carron R and Williamson A 2021 Orientation of temporal interference for non-invasive deep brain stimulation in epilepsy *Front. Neurosci.* **15** 633988
[31] Bikson M, Inoue M, Akiyama H, Deans J K, Fox J E, Miyakawa H and Jefferys J G R 2004 Effects of uniform extracellular DC electric fields on excitability in rat hippocampal slices in vitro *J. Physiol.* **557** 175–90
[32] Deans J K, Powell A D and Jefferys J G R 2007 Sensitivity of coherent oscillations in rat hippocampus to AC electric fields *J. Physiol.* **583** 555–65
[33] Song X, Zhao X, Li X, Liu S and Ming D 2021 Multi-channel transcranial temporally interfering stimulation (tTIS): application to living mice brain *J. Neural Eng.* **18** 036003
[34] Yatsuda K, Yu W and Gomez-Tames J 2024 Population-level insights into temporal interference for focused deep brain neuromodulation *Front. Hum. Neurosci.* **18** 1308549
[35] Rampersad S, Roig-Solvas B, Yarossi M, Kulkarni P P, Santarnecchi E, Dorval A D and Brooks D H 2019 Prospects for transcranial temporal interference stimulation in humans: a computational study *NeuroImage* **202** 116124
[36] Zhu X, Li Y, Zheng L, Shao B, Liu X, Li C, Huang Z-G, Liu T and Wang J 2019 Multi-point temporal interference stimulation by using each electrode to carry different frequency currents *IEEE Access* **7** 168839–48
[37] Lee S, Park J, Choi D S, Lee C and Im C-H 2022 Multipair transcranial temporal interference stimulation for improved focalized stimulation of deep brain regions: a simulation study *Comput. Biol. Med.* **143** 105337
[38] Bevacqua M T, Gaffoglio R, Bellizzi G G, Righero M, Giordanengo G, Crocco L, Vecchi G and Isernia T 2023 Field and temperature shaping for microwave hyperthermia: recent treatment planning tools to enhance SAR-based procedures *Cancers* **15** 1560
[39] Sales D C 1983 An investigation into the potential of microwave radiant energy as a source of heating for human comfort *Build. Serv. Eng. Res. Technol.* **4** 84–96
[40] Strigo I A, Carli F and Bushnell M C 2000 Effect of ambient temperature on human pain and temperature perception *Anesthesiology* **92** 699–707
[41] Carpenter D O 2015 The microwave syndrome or electro-hypersensitivity: historical background *Rev. Environ. Health* **30** 217–22
[42] Hardell L and Nilsson M 2025 Summary of seven Swedish case reports on the microwave syndrome associated with 5G radiofrequency radiation *Rev. Environ. Health* **40** 147–57
[43] Begum J 2024 Electromagnetic Hypersensitivity (available at: www.webmd.com/a-to-z-guides/electromagnetic-hypersensitivity)
[44] Noetscher G M, Serano P, Wartman W A, Fujimoto K and Makarov S N 2021 Visible Human Project® female surface based computational phantom (Nelly) for radio-frequency safety evaluation in MRI coils *PLoS One* **16** e0260922
[45] Makarov S N, Noetscher G M, Yanamadala J, Piazza M W, Louie S, Prokop A, Nazarian A and Nummenmaa A 2017 Virtual human models for electromagnetic studies and their applications *IEEE Rev. Biomed. Eng.* **10** 95–121

[46] Iacono M I *et al* 2015 MIDA: a multimodal imaging-based detailed anatomical model of the human head and neck *PLoS One* **10** e0124126
[47] Rayleigh L 1896 On the theory of optical images, with special reference to the microscope *Phil. Mag.* **42** 167–95
[48] Pennes H H 1948 Analysis of tissue and arterial blood temperatures in the resting human forearm *Appl. Physiol.* **1** 93–122
[49] Bernardi P, Cavagnaro M, Pisa S and Piuzzi E 2000 Specific absorption rate and temperature increases in the head of a cellular-phone user *IEEE Trans. Microw. Theory Tech.* **48** 1118–26
[50] Abdulrasool A A, Abbas A K and Abdullah W N 2023 The cooling effect of blood flow during hyperthermia treatment *J. Therm. Biol.* **114** 103581
[51] Yaghmazadeh O, Vöröslakos M, Alon L, Carluccio G, Collins C, Sodickson D K and Buzsáki G 2022 Neuronal activity under transcranial radio-frequency stimulation in metal-free rodent brains in-vivo *Commun. Eng.* **1** 15
[52] Cassel J-C, Cosquer B, Galani R and Kuster N 2004 Whole-body exposure to 2.45 GHz electromagnetic fields does not alter radial-maze performance in rats *Behav. Brain Res.* **155** 37–43
[53] Cobb B L, Jauchem J R and Adair E R 2004 Radial arm maze performance of rats following repeated low level microwave radiation exposure *Bioelectromagnetics* **25** 49–57
[54] Yang C, Veit N C, McKenzie K A, Aalla S, Kishta A, Embry K, Roth E J, Lieber R L and Jayaraman A 2025 The effects of stimulation waveform and carrier frequency on tolerance and motor thresholds elicited by transcutaneous spinal cord stimulation in stroke *Clin. Neurophysiol. Pract.* **10** 150–8
[55] Ansari M A, Zarei M, Akhlaghipour N and Niknam A R 2017 Skull and cerebrospinal fluid effects on microwave radiation propagation in human brain *J. Phys. D: Appl. Phys.* **50** 495401
[56] Xue C, Zhou G and Wong A M H 2024 Metasurface approach to generate homogeneous B_1^+ field for high-field and ultra-high-field MRI *IEEE J. Electromagn. RF Microw. Med. Biol.* **8** 155–62
[57] IEEE International Committee on Electromagnetic Safety 2019 IEEE standard for safety levels concerning human exposure to radio frequency electromagnetic fields, 3 kHz–300 GHz IEEE Std C95.1-2019 (Revision of IEEE Std C95.1-2005) pp 1–238
[58] IT'IS foundation 2010–25 *Database summary of tissue properties* (available at: https://itis.swiss/virtual-population/tissue-properties/database/database-summary/)
[59] Fanori L, Liscidini A and Castello R 2010 3.3 GHz DCO with a frequency resolution of 150 Hz for All-digital PLL *2010 IEEE Int. Solid-State Circuits Conf. (ISSCC)* pp 48–49
[60] Mariak Z, White M D, Lewko J, Lyson T and Piekarski P 1999 Direct cooling of the human brain by heat loss from the upper respiratory tract *J. Appl. Physiol.* **87** 1609–13
[61] Lyons B E, Samulski T V, Cox R S and Fessenden P 1989 Heat loss and blood flow during hyperthermia in normal canine brain. I: empirical study and analysis *Hyperthermia* **5** 225–47
[62] Fenn A J and King G A 1996 Experimental investigation of an adaptive feedback algorithm for hot spot reduction in radio-frequency phased-array hyperthermia *IEEE Trans. Biomed. Eng.* **43** 273–80
[63] Aldhaeebi M, Alzabidi M and Elshafiey I 2013 Genetic algorithm optimization of SAR distribution in hyperthermia treatment of human head *1st Int. Conf. on Artificial Intelligence, Modelling and Simulation* vol 2013 pp 92–97
[64] Yildiz G, Yasar H, Uslu I E, Demirel Y, Akinci M N, Yilmaz T and Akduman I 2022 Antenna excitation optimization with deep learning for microwave breast cancer hyperthermia *Sensors* **22** 6343
[65] Yi G-S, Wang J, Deng B and Wei X-L 2017 Morphology controls how hippocampal CA1 pyramidal neuron responds to uniform electric fields: a biophysical modeling study *Sci. Rep.* **7** 3210
[66] Halliday G M 2009 Thalamic changes in Parkinson's disease *Parkinsonism Related Disord.* **15** S152–5
[67] Lin H C, Wu Y H and Ker M D 2025 Modulation of local field potentials in the deep brain of minipigs through transcranial temporal interference stimulation *Neuromodulation* **28** 434–43
[68] Zanoli M, Ek E and Dobšíček Trefná H 2023 Antenna arrangement in UWB helmet brain applicators for deep microwave hyperthermia *Cancers* **15** 1447
[69] Dongus S, Jalilian H, Schürmann D and Röösli M 2022 Health effects of WiFi radiation: a review based on systematic quality evaluation *Crit. Rev. Environ. Sci. Technol.* **52** 3547–66
[70] Micheli D, Delfini A, Santoni F, Volpini F and Marchetti M 2014 Measurement of electromagnetic field attenuation by building walls in the mobile phone and satellite navigation frequency bands *IEEE Antennas Wirel Propag. Lett.* **14** 698–702
[71] Findlay R P and Dimbylow P J 2010 SAR in a child voxel phantom from exposure to wireless computer networks (Wi-Fi) *Phys. Med.* **55** N405
[72] Sârbu A, Miclăuș S, Digulescu A and Bechet P 2020 Comparative analysis of user exposure to the electromagnetic radiation emitted by the fourth and fifth generations of Wi-fi communication devices *Int. J. Environ. Res. Public Health* **17** 8837
[73] Buckus R, Strukcinskiene B and Raistenskis J 2014 The assessment of electromagnetic field radiation exposure for mobile phone users *Vojnosanit Pregl* **71** 1138–43
[74] Hüppi P S, Warfield S, Kikinis R, Barnes P D, Zientara G P, Jolesz F A, Tsuji M K and Volpe J J 1998 Quantitative magnetic resonance imaging of brain development in premature and mature newborns *Ann. Neurol.* **43** 224–35
[75] Jäncke L, Mérillat S, Liem F and Hänggi J 2015 Brain size, sex, and the aging brain *Hum. Brain Mapp* **36** 150–69
[76] Raz N *et al* 1997 Selective aging of the human cerebral cortex observed *in vivo*: differential vulnerability of the prefrontal gray matter *Cereb. Cortex* **7** 268–82
[77] Ruigrok A N V, Salimi-Khorshidi G, Lai M-C, Baron-Cohen S, Lombardo M V, Tait R J and Suckling J 2014 A meta-analysis of sex differences in human brain structure *Neurosci. Biobehav. Rev.* **39** 34–50
[78] Cosgrove K P, Mazure C M and Staley J K 2007 Evolving knowledge of sex differences in brain structure, function, and chemistry *Biol. Psychiatry* **62** 847–55
[79] Gur R E and Gur R C 1990 Gender differences in regional cerebral blood flow *Schizophr. Bull.* **16** 247–54
[80] Donahue K M, Krouwer H G J, Rand S D, Pathak A P, Marszalkowski C S, Censky S C and Prost R W 2000 Utility of simultaneously acquired gradient-echo and spin-echo cerebral blood volume and morphology maps in brain tumor patients *Magn. Reson Med.* **43** 845–53
[81] Ilkhomovna K M, Eriyigitovich I S and Kadyrovich K N 2020 Morphological features of microvascular Tissue of the Brain at hemorrhagic stroke *Am. J. Med. Sci. Pharm. Res.* **2** 53–59